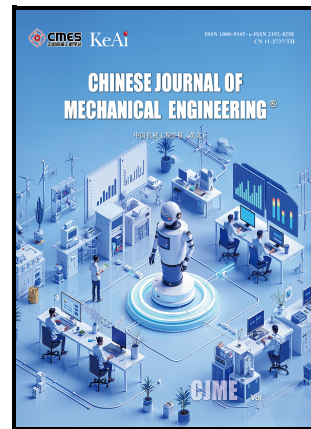


Journal Pre-proof

Whole-Body Trajectory Optimization for Skid Steer Wheeled-Legged Vehicles

Mingfan Xu, Ziyi Yang, Chuyan Xu, Kui Wang,
Yu Zhang, Yechen Qin



PII: S1000-9345(25)00132-4

DOI: <https://doi.org/10.1016/j.cjme.2025.100128>

Reference: CJME100128

To appear in: *Chinese Journal of Mechanical Engineering*

Received date: 3 May 2025

Revised date: 28 August 2025

Accepted date: 17 October 2025

Please cite this article as: Mingfan Xu, Ziyi Yang, Chuyan Xu, Kui Wang, Yu Zhang and Yechen Qin, Whole-Body Trajectory Optimization for Skid Steer Wheeled-Legged Vehicles, *Chinese Journal of Mechanical Engineering*, (2025) doi:<https://doi.org/10.1016/j.cjme.2025.100128>

This is a PDF file of an article that has undergone enhancements after acceptance, such as the addition of a cover page and metadata, and formatting for readability, but it is not yet the definitive version of record. This version will undergo additional copyediting, typesetting and review before it is published in its final form, but we are providing this version to give early visibility of the article. Please note that, during the production process, errors may be discovered which could affect the content, and all legal disclaimers that apply to the journal pertain.

© 2025 Published by Elsevier.

ORIGINAL ARTICLE

Whole-Body Trajectory Optimization for Skid Steer Wheeled-Legged Vehicles

Mingfan Xu¹, Ziyi Yang¹, Chuyan Xu¹, Kui Wang¹, YuZhang¹ and Yechen Qin^{1,*}

Abstract

Wheel-legged vehicles combine the advantage of high-speed capability of wheeled locomotion with the superior mobility of legged mechanisms, demonstrating exceptional performance in structured environments. However, these hybrid systems face several challenges regarding energy efficiency and motion control complexity when operating in unstructured terrains. To address these challenges, this study proposes a real-time whole-body trajectory optimization framework, designed for wheel-legged hybrid vehicles, with optimized performance in challenging environments, such as staircases, slopes, and construction sites. The proposed framework innovatively integrates the obstacle negotiation capability of legged robots with the slip-steering advantage of wheeled platforms, providing distinctive benefits for various applications, including search-and-rescue missions and planetary exploration. Unlike conventional wheel-legged designs, the proposed LegoWheel platform incorporates a streamlined mechanical architecture that eliminates redundant hip abduction-adduction (HAA) joints while realizing steering through differential wheel speed control. The unified optimization framework simultaneously considers wheeled and legged dynamics, providing optimal trajectories for joints and wheels, while addressing body motion, contact forces, and wheel torque distribution. The proposed framework is verified by extensive experiments across various challenging terrains, including staircases and trenches. The results demonstrate that the proposed LegoWheel can achieve significant improvements in energy efficiency for specific operational scenarios compared to traditional wheel-legged robots, while maintaining the robust obstacle-crossing feature and high-speed stability. The key innovations of this study include: (1) an innovative minimalist wheel-legged architecture that reduces mechanical complexity; (2) a unified optimization framework for hybrid locomotion dynamics; and (3) experimental validation of energy-efficient navigation in real-world unstructured environments. These advancements collectively enhance operational efficiency and performance in demanding conditions.

Keywords: Wheeled-legged vehicle, Skid steer, Trajectory optimization, Optimal control

1 Introduction

Wheeled-legged hybrid platforms exhibit superior performance in terms of the movement speed, terrain adaptability, and transportation efficiency compared to single-mode unmanned ground vehicles [1,2]. Due to the mentioned advantages, these platforms are particularly suitable for challenging operational scenarios, such as urban last-mile delivery in complex road environments and disaster relief missions in unstructured terrains. For instance, recent deployments in post-earthquake rescue operations have demonstrated the ability of these vehicles to navigate through rubble while ensuring stable payload transportation. Recently, the integration of wheels and legs has become a prominent research focus in the field of mobile robotics [3], particularly for applications requiring both mobility and manipulation capabilities in semi-structured environments.

Furthermore, recent advances in skid-steering vehicle dynamics have substantially improved the understanding of wheel-terrain interaction mechanisms. For instance, Kim et al. [4] developed an autonomous navigation algorithm that combines skid steering with pure pursuit methods through compensation coefficients. Their work highlighted the importance of considering slip dynamics in vehicle control. Similarly, Hao et al. [5] proposed a wheel-centered trajectory planning method designed specifically for wheel-legged robots, which demonstrated improved steering performance through optimized torque distribution.

*Correspondence: qinyechen@bit.edu.cn

¹ School of Mechanical Engineering, Beijing Institute of Technology, Beijing 100081, China
Full list of author information is available at the end of the article

To address the model predictive control for skid-steer vehicles, Dorbetkhany et al. [6] developed a spatial-based MPC approach that could achieve robust path following while accounting for kinematic constraints. Kang et al. [7] further contributed to this field by designing a linear lateral motion model for urban delivery robots and conducting the stability analysis under various operating conditions, which provided valuable insights. The latest work of Martínez et al. [8] extended these concepts to sloped terrains by proposing an ICR-based kinematic model that accounted for firm slope conditions.

Current research on wheeled-legged platforms mainly focuses on robotic applications, particularly considering their dynamic obstacle-crossing capabilities and indoor functional demonstrations [9,10]. However, fewer studies have investigated the wheel dynamics of wheeled-legged platforms [1], particularly the tire forces induced by wheel slip during locomotion, which could significantly impact the overall vehicle dynamics. Recent studies conducted by Trivedi et al. [11] and Tan et al. [12] have demonstrated the importance of probabilistic motion modeling and integrated control algorithms for skid-steer vehicles operating on off-road terrains.

The field of trajectory optimization for hybrid locomotion systems has experienced notable advancements in recent years. Effati et al. [13] formulated an equivalent time-optimal problem to plan energy-efficient paths for skid-steer rovers. Xiong et al. [14] developed a cascaded NTSM-PID control method to improve the path-tracking performance. Zuo et al. [15] further enhanced visual-based kinematics estimation for skid-steering robots by addressing the challenge of pose estimation during dynamic maneuvers.

In outdoor special environments, vehicles must maneuver at high speeds over complex terrain while carrying a defined payload. In addition, traditional four-wheeled legged platforms typically require hip abduction/adduction (HAA) joints to provide lateral torque during steering, which necessitates four additional motorized swing joints [16]. However, this configuration cannot ensure equal lateral forces on both sides of the wheels during high-speed driving, thus requiring constant adjustments via the HAA motors to maintain track width. This not only increases vehicle weight but also causes higher energy consumption. Recent developments in transformable wheel-leg mechanisms [17,18] and hybrid locomotion strategies [19] have provided promising alternatives to conventional designs.

Moreover, in high-speed operations, due to the presence of legged structures, the platform's height requires large torque from the HAA motors to maintain stability [20], which increases the requirements for motor drive capacity. Recent research on posture adjustment [21] and compliant motion control [22] has introduced several improved approaches for maintaining stability in wheel-legged systems. The development of multimodal locomotion platforms, such as MAX [23] and SKATER [24], further illustrates the potential of integrated control strategies for achieving both high-speed stability and terrain adaptability.

Furthermore, the wheel's lifting off the ground during the steering process decreases platform stability, which hinders efficient maneuvering in complex scenarios. Recent advances in trajectory optimization formulations [25] have addressed this problem by providing smooth analytical derivatives for both wheeled and legged modes of operation, thus enabling more efficient transitions between locomotion modes.

Recent studies have presented various quadruped robots equipped with passive wheels that can achieve wheel-skid locomotion. For instance, through force control, the ANYmal robot with passive wheels [26] can perform skating gaits and glide across both flat and inclined terrains. Similarly, by implementing decoupled control of foot position and passive wheel yaw angle, the QSskater-E robot [27] can realize various motion patterns, including swizzling, strokes, and jogging gaits. The advanced ANYmal platform [28] with active torque-controlled wheels uses a moving contact point model with kinematic constraints for wheel dynamics. This system employs model predictive control (MPC) for offline trajectory optimization combined with inverse dynamics for motion tracking.

Recent research on reinforcement learning (RL) application to motion control of wheeled-legged robots has achieved significant progress. Generally, the RL-based approaches require sophisticated reward function engineering to achieve desired locomotion patterns. The ANYmal robot [29] employs an RL framework based on adversarial motion learning, which enables multiple discrete and switchable gaits. These behaviors are achieved through skills transferred from the existing RL controllers (e.g., obstacle avoidance and walking) along with seamless transitions between quadrupedal and humanoid configurations. Both the Lynx [30] and Unitree B2W [31] robots can achieve remarkable dynamic stability in mountainous terrains using RL-based mechanisms.

Although RL-based methods can generate efficient motion policies without explicit terrain perception, they face some limitations in environments with cracks or uneven surfaces, where wheels may get trapped in crevices, which can potentially lead to hazardous situations [32]. Moreover, the implementation of RL-based approaches demands extensive training data

and suffers from slow convergence rates. Current simulation platforms face various challenges, particularly in accurately modeling wheel-terrain interactions during tire slippage scenarios, thus making sim-to-real transfer especially challenging for skid-steering vehicles.

In contrast, traditional MPC methods can effectively obtain locally optimal solutions for structured terrains while ensuring good generalization ability across diverse environments. These model-based approaches use explicit mathematical formulations to handle constraints effectively, thus providing robust stability guarantees and control performance. However, they require precise system modeling and substantial computational resources, which pose significant challenges, particularly for complex or unknown systems.

This study evaluates system performance using three quantifiable metrics: (1) stability, measured by the absence of tipping events during system operation, (2) energy efficiency, calculated via electrical consumption during standardized tasks, and (3) terrain adaptability, quantified by maximum surmountable obstacle height, negotiable slope angle, and trench crossing length.

Compared to the existing approaches, the proposed framework has three main improvements. First, compared to the model-based MPC methods [20,28], the proposed skid-steering mechanism eliminates the HAA joints while achieving smoother steering through integrated tire dynamics; it also demonstrates a 43.22% reduction in the total motor energy consumption during in-place turning scenarios. Second, compared to the passive-wheel systems [26,27], the active torque control architecture of the proposed method enables higher tracking precision through real-time slip regulation and adaptive force distribution, while preserving full obstacle clearance capability.

The main contributions of this work can be summarized as follows:

- A real-time optimal control framework is proposed for an advanced vehicle configuration, which integrates legged and wheeled dynamics within a unified whole-body trajectory optimization scheme for skid steering wheeled-legged platforms. This approach ensures coordinated optimization of both locomotion modalities. The proposed algorithm can simultaneously optimize all control variables required for trajectory tracking, supporting both basic linear and angular velocity commands (for perception-free remote operation) and customized trajectory following in specific terrains, thus significantly expanding the repertoire of executable complex maneuvers.
- The proposed model incorporates wheel-terrain interaction dynamics and skid-steering mechanisms. In addition, the implemented contact-based steering system, derived from skid-steering kinematics, demonstrates superior motion smoothness and operational speed compared to conventional lift-leg steering approaches.
- The results of comprehensive experimental validation demonstrate high effectiveness of the proposed framework across multiple scenarios, including precise velocity tracking, successful navigation through complex three-dimensional (3D) terrains (25° slopes, stairs, and trenches), significant energy savings compared to the traditional abduction-joint approaches (up to 52.33% and 43.22% reduction in straight-line motion and spot turning, respectively, and robust performance in perception-free operation modes).

2 Modeling

Wheeled-legged vehicles represent multimodal systems that combine wheeled and legged mechanisms. The proposed trajectory optimization algorithm integrates five sub-models of wheeled-legged vehicles, as shown in Figure 1. The five models include: the single rigid-body dynamics model, the full kinematics model, the wheel dynamics model, the tire model, and the skid-steering kinematics model. The five models account for different aspects of a vehicle's motion: centroidal dynamics, leg kinematics, wheel dynamics, wheel-ground interaction, and skid-steering kinematics. The five models are explained in detail in the following sections.

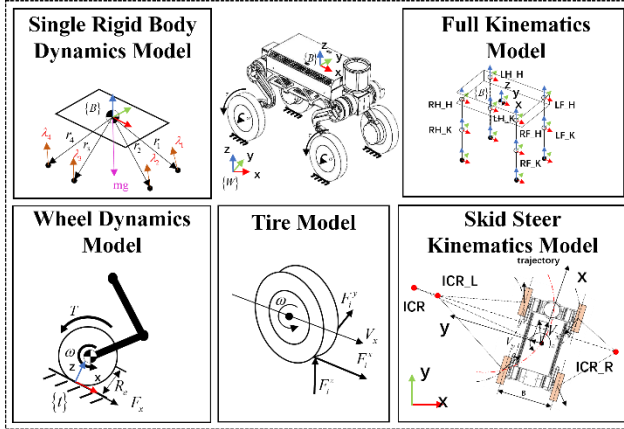


Figure 1 The coordinate frames and integrated models of a wheeled-legged vehicle.

2.1 Single Rigid-Body Dynamics Model

The dynamics model is formulated using two reference frames: the world coordinate system (WCS) and the body-fixed frame (BFF). The WCS is an inertial frame whose z -axis is aligned opposite to gravity. The BFF is attached to the center of mass (CoM) of a vehicle, and its axes are aligned with the principal axes of inertia. The transformations between these frames are performed using a rotation matrix $\mathbf{R}(\theta)$ derived from attitude angles θ .

Centroidal dynamics are critical for controlling the motion of a vehicle's CoM. In addition, a single rigid-body dynamics model is adopted to describe the CoM dynamics. The linear and angular accelerations of the CoM are respectively defined as follows:

$$\mathbf{v} = \mathbf{g}(\theta) + \frac{1}{m} \sum_{i=1}^4 \lambda_i, \quad (1)$$

$$\dot{\omega} = \mathbf{I}^{-1}(\mathbf{q}) \left(\dot{\mathbf{I}}(\mathbf{q}, \mathbf{u}) \cdot \omega \times \mathbf{I}(\mathbf{q})\omega + \sum_{i=1}^4 \mathbf{r}_{f_i}(\mathbf{q}) \times \lambda_i \right), \quad (2)$$

where \mathbf{v} and ω correspond to the linear and angular velocities of a vehicle in the world coordinate system; \mathbf{g} is the gravitational acceleration in the world coordinate system; m is the total mass of the rigid body; \mathbf{I} is the moment of inertia about the CoM; λ_i is the contact force between the wheel and the ground in the global frame; \mathbf{r}_{f_i} represents the position of the center-of-wheel (CoW) and is derived from the CoW kinematics; \mathbf{q} is the generalized coordinate vector, expressed as follows:

$$\mathbf{q} = \begin{bmatrix} \mathbf{p} \\ \theta \\ \mathbf{q}_j \end{bmatrix}, \quad (3)$$

where \mathbf{p} and θ denote the position and attitude angle of a vehicle in the world coordinate system; \mathbf{q}_j represents the joint angles of a leg, including the hip and knee joints.

2.2 Full Kinematics Model

To constrain the CoW, it is necessary to determine the CoW's position and velocity using a kinematics model. The wheeled-legged vehicle kinematics can be expressed as follows:

$$\mathbf{r}_{f_i} = f(\mathbf{q}), \quad (4)$$

$$\mathbf{v}_{f_i} = \mathbf{J}_v(\mathbf{q})\dot{\mathbf{q}}, \quad (5)$$

where \mathbf{v}_{f_i} represents the velocity of the CoW, and \mathbf{J}_v is the Jacobian matrix that maps joint velocities to the CoW velocities.

2.3 Wheel Dynamics Model

The rotational dynamics of the wheels are governed by the following expression:

$$\frac{T_i - I_w \dot{\omega}_i}{r_w} = (^t \mathbf{R}_w \lambda_i)_1, \quad (6)$$

where T_i is the wheel torque; I_w is the rotational inertia of the wheel; ω_i is the wheel speed; r_w is the wheel radius; $(\cdot)_1$ is the first element of a vector; ${}^t \mathbf{R}_w$ is the rotation matrix that transforms the contact force from the world coordinate system to the terrain coordinate system of a leg i ; $({}^t \mathbf{R}_w \lambda_i)_1$ represents the contact force in the direction of the wheel's forward motion, and in the absence of terrain perception, this matrix can be assumed to be the identity matrix or estimated through the state estimation to fit specific terrain.

2.4 Tire Model

The motion of a wheeled-legged vehicle is primarily driven by the interaction forces between the vehicle's tires and the ground, which include frictional forces and normal forces.

The tire forces are modeled as follows:

$$\begin{cases} F_i^x = C_x s_i, \\ F_i^y = C_y \alpha_i, \end{cases} \quad (7)$$

where F_i^x and F_i^y are the tire forces in the longitudinal and lateral directions of the wheel, respectively, and they are obtained in the same manner as the tire forces in Eq. (6); C_x and C_y are the longitudinal and lateral stiffness coefficients, respectively; α is the slip angle; s is the longitudinal slip ratio.

2.5 Skid Steer Kinematics Model

During the contact phase, the kinematic model for tire slip is defined as follows [33]:

$$\begin{cases} V_x = \frac{r_w}{2} [w_{1,3}(1-s_{1,3}) + w_{2,4}(1-s_{2,4})], \\ V_y = \frac{r_w}{2} [w_{1,3}(1-s_{1,3}) + w_{2,4}(1-s_{2,4})] \tan \beta, \\ \omega_z = \frac{r_w [-w_{1,3}(1-s_{1,3}) + w_{2,4}(1-s_{2,4})]}{B}. \end{cases} \quad (8)$$

where V_x and V_y are the longitudinal and lateral velocities in the vehicle coordinate system, respectively; r_w is the wheel radius; B is the wheeltrack; β is the sideslip angle of the vehicle body.

3 Trajectory Optimization

This study employs a nonlinear switched-system MPC framework to effectively address the constraints caused by wheel lift-off during platform motion, as shown in Figure 2. The system dynamics are divided into 16 distinct subsystems according to the individual wheel-ground contact conditions. The switching sequence between these subsystems is determined by either predefined gait patterns or an NLP-based optimization approach, as described in Ref. [34].

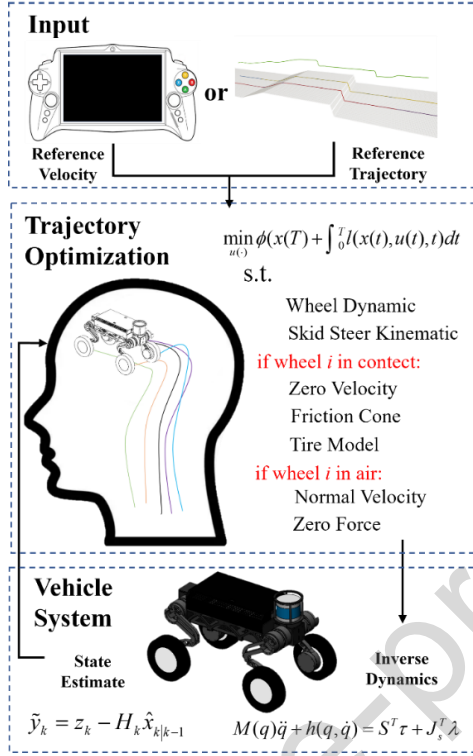


Figure 2 The control architecture of a wheeled-legged vehicle.

3.1 MPC Framework

The nonlinear model predictive control framework consists of six core components:

- Objective function defined by Eq. (9), which combines the terminal and running costs;
- System dynamics constraint given by Eq. (10);
- Initial condition constraint expressed by Eq. (11);
- State-input equality constraints defined by Eq. (12);
- Pure state equality constraints given by Eq. (13);
- Inequality constraints expressed by Eq. (14).

The optimization problem is formulated as follows:

$$\min_{u(\cdot)} \phi(x(T)) + \int_0^T l(x(t), u(t), t) dt, \quad (9)$$

$$\text{subject to } \dot{x}(t) = f(x(t), u(t), t), \quad (10)$$

$$x(0) = \{x_0\}, \quad (11)$$

$$\{g_{-1}\}(x(t), u(t), t) = 0, \quad (12)$$

$$\{g_{-2}\}(x(t), t) = 0, \quad (13)$$

$$h(x(t), u(t), t) \geq 0. \quad (14)$$

where T is the receding horizon; $x(t)$ is the state vector; $u(t)$ is the control input vector; $l(\cdot)$ is the running cost; $\phi(\cdot)$ is the terminal cost.

3.2 System Dynamics

To implement the model predictive control for this system, this study employs the switched-system MPC algorithm, whose pseudo-code is presented in Algorithm 1. This algorithm can handle the contact state transitions and gait patterns. In addition, to accurately represent a vehicle's motion and dynamics, this study adopts a simplified yet effective approach for system modeling. This study models the system dynamics considering both the CoM dynamics and full kinematics. The system model consists of 24 state variables, describing the CoM motion, joint positions, and wheel speeds. The model has 28 control inputs, including the tire-ground contact forces in the world coordinate frame, joint velocities, wheel accelerations, and

wheel torques. The state variables are all measurable, whereas the input variables are all unmeasurable.

Algorithm 1 Switched-System MPC for Wheeled-Legged Vehicles

Require: Initial state x_0 , reference trajectory x_{ref} , horizon T
Ensure: Optimal control sequence U^*

- 1: Initialize: $t \leftarrow 0, x \leftarrow x_0$
- 2: Load gait pattern \mathcal{G} (predefined)
- 3: **while** $t < T_{total}$ **do**
- 4: **1. Contact Detection:**
- 5: $\sigma \leftarrow \text{DetectContactState}(x)$ \triangleright Get current subsystem
- 6: **2. Constraint Setup:**
- 7: **if** using gait pattern \mathcal{G} **then**
- 8: $g_\sigma, h_\sigma \leftarrow \text{LoadGaitConstraints}(\mathcal{G}, t)$
- 9: **else**
- 10: $g_\sigma, h_\sigma \leftarrow \text{BuildNLPConstraints}(x)$
- 11: **end if**
- 12: **3. Dynamics Linearization:**
- 13: $A, B \leftarrow \text{LinearizeDynamics}(f_\sigma, x, u_{prev})$
- 14: **4. SLQ Optimization:**
- 15: $U^* \leftarrow \text{SolveSLQ}(A, B, Q, R, g_\sigma, h_\sigma)$
- 16: **5. Control Application:**
- 17: $\text{ApplyControl}(U^*[0])$ \triangleright Apply first control input
- 18: **6. State Prediction:**
- 19: $x_{next} \leftarrow \text{PredictState}(x, U^*[0], \Delta t)$
- 20: **7. Time Update:**
- 21: $t \leftarrow t + \Delta t$
- 22: $x \leftarrow x_{next}$
- 23: **end while**
- 24: **return** U^*

The state and input variables are defined as follows:

$$x(t) = [v^\top \quad \omega^\top \quad p^\top \quad \theta^\top \quad q_j^\top \quad w_i^\top]^\top \in \mathbb{R}^{12+n_j+n_i}, \quad (15)$$

$$u(t) = [\lambda_i^\top \quad u_j^\top \quad a_i^\top \quad T_i^\top]^\top \in \mathbb{R}^{3n_e+2n_i+n_j}, \quad (16)$$

where n_j is the number of joints, and $n_j = 8$; n_i is the number of wheels, and $n_i = 4$; n_e is the number of legs, and $n_e = 4$; u_j^\top is the joint speed; a_i^\top is the wheel acceleration.

The system motion equations are expressed as follows:

$$\begin{cases} \dot{v} = g(\theta) + \frac{1}{m} \sum_{i=1}^4 \lambda_i, \\ \dot{\omega} = I^{-1}(q)(I(q, u) \cdot \omega \times I(q)\omega + \sum_{i=1}^4 r_{fi}(q) \times \lambda_i), \\ \dot{p} = R(\theta)v, \\ \dot{\theta} = {}^W T_B(\theta)(\omega - B J_{com}^\omega(q)u), \\ \dot{q}_j = u_j, \\ \dot{w}_i = a_i. \end{cases} \quad (17)$$

where R is the rotation matrix representing the body's orientation relative to the world coordinate system, as depicted in Figure 1; ${}^W T_B$ is a matrix that transforms the angular velocities in the base frame to the Euler angles derivatives in the global frame; $B J_{com}^\omega$ is the Jacobian matrix of the CoM rotation with respect to the vehicle's base frame.

3.3 Cost Function

The proposed motion controller features a general interface, allowing users to track the speed in the pure wheeled mode, execute various standard gaits in the legged mode, and follow custom-designed hybrid wheel-leg gaits and desired trajectories. This flexibility is ensured by defining different reference trajectories. The reference trajectories can either be pre-generated using trajectory planning methods, such as the method proposed in Ref. [34], or derived from the desired CoM

linear and angular velocities over a planning horizon T , along with the joint trajectories calculated from nominal configurations. The cost function at a time t is computed as follows:

$$l(x(t), u(t), t) = \frac{1}{2} \tilde{x}(t)^T Q \tilde{x}(t) + \frac{1}{2} \tilde{u}(t)^T R \tilde{u}(t). \quad (18)$$

Physical Interpretation:

State Tracking Term ($\tilde{x}^T Q \tilde{x}$): This term penalizes deviations from the reference trajectory, where $\tilde{x}(t) = x(t) - x_{ref}(t)$ captures tracking errors in the CoM position or orientation, joint angles, and wheel speeds. Diagonal elements of Q determine relative importance of different state variables; for instance, higher weights for the CoM position than for the joint angles.

Control Effort Term ($\tilde{u}^T R \tilde{u}$): This term regularizes control inputs to prevent excessive actuation, where $\tilde{u}(t) = u(t) - u_{ref}(t)$ represents deviations from nominal control inputs, and the coefficients of matrix R define trade-offs between different actuators (e.g., wheel torques vs. joint velocities).

The reference trajectories can be generated through two distinct approaches:

(1) Velocity-based Mode: For wheel-dominated locomotion, references are computed from desired velocities using the skid steer kinematics model;

(2) Trajectory Optimization Mode: For complex maneuvers, pre-computed optimal trajectories from Ref. [34] provide full state references

3.4 Reference Trajectory

The proposed controller features multiple input interfaces due to the specific formulation of its cost function. The switching system is divided into 16 subsystems based on the foot contact conditions. Moreover, gait patterns are defined by configuring the switching system and transition timing to determine the leg contact states and durations. Furthermore, the trot gait is designed to alternate between subsystems 9 and 16 with a switching period of 0.8 s.

When using the desired velocity v_{des} , angular velocity ω_{des} , and gait pattern as inputs, the reference trajectory $x(t)$ is defined as follows:

$$\mathbf{p}_{ref} = \mathbf{p}_{curr} + \mathbf{R} \cdot v_{des} \cdot T, \quad (19)$$

$$\theta_{ref} = \theta_{curr} + \omega_{des} \cdot T, \quad (20)$$

$$\mathbf{q}_i^{ref} = \mathbf{q}_i^{default}, \quad (21)$$

$$w_i^{ref} = \begin{cases} (2v_{des}^x - \omega_{des}^z B) / 2r_w, \\ (2v_{des}^x + \omega_{des}^z B) / 2r_w. \end{cases} \quad (22)$$

where \mathbf{p}_{curr} is the current position, θ_{curr} is the current orientation angle, and $\mathbf{q}_i^{default}$ indicates the joint angles in the default standing posture.

To enhance computational efficiency, this study derived the desired wheel speeds using simplified skid steering kinematics. In addition, for the NLP-based input mode, the high-level planner generates all required state variables for MPC along with the subsystem switching schedules. Consequently, the offline trajectories can be directly used as reference trajectories.

3.5 Asymptotic Stability Analysis

To prove asymptotic stability of the proposed switched-system MPC framework, this study employs Lyapunov's direct method with extensions for varying terrain conditions.

Consider a nonlinear switched-system MPC framework defined by Eqs. (9)–(14) as follows:

- 1) Positive definite running cost $l(x, u, t)$ is calculated by Eq. (18);
- 2) Terminal cost $\phi(x(T))$ is designed as a local Lyapunov function;
- 3) Terminal constraint set \mathcal{X}_f satisfying the following condition:

$$f(x, \kappa_f(x)) \in \mathcal{X}_f, \forall x \in \mathcal{X}_f; \quad (23)$$

- 4) The terrain parameters satisfying Lipschitz condition given by:

$$\|\mu(\mathbf{p}_1) - \mu(\mathbf{p}_2)\| \leq L_\mu \|\mathbf{p}_1 - \mathbf{p}_2\|; \quad (24)$$

- 5) Slip dynamics are governed by:

$$\dot{s}_i = -\frac{1}{\tau_s} s_i + \frac{1}{\tau_s} \sigma(\mathbf{p}, \boldsymbol{\omega}) . \quad (25)$$

Then, the closed-loop system is asymptotically stable within the boundaries defined by:

$$\bar{\mu} \leq \frac{\alpha}{\beta L_\mu} \sqrt{\frac{\lambda_{\min}(Q)}{\lambda_{\max}(P)}} . \quad (26)$$

Proof:

Step 1: Lyapunov Candidate Function

Define the optimal value function as follows:

$$V^*(x(t)) = \phi(x^*(T)) + \int_t^T l(x^*(\tau), u^*(\tau), \tau) d\tau, \quad (27)$$

where $x^*(\tau)$ and $u^*(\tau)$ denote the optimal trajectories.

The positive definiteness follows from the following expression:

$$l(x, u, t) \geq \alpha_1(\|x\|), \phi(x(T)) \geq \alpha_2(\|x(T)\|); \quad (28)$$

Step 2: Decrement Property

At a time t , let $\{u^*(\tau)\}_{\tau=t}^{t+T}$ be the optimal control sequence and construct a feasible control sequence for $(t + \Delta t)$ as follows:

$$\tilde{u}(\tau) = \begin{cases} u^*(\tau) & \tau \in [t + \Delta t, t + T], \\ \kappa_f(x) & \tau = t + T. \end{cases} \quad (29)$$

The suboptimality yields the following expression:

$$\begin{aligned} V^*(x(t + \Delta t)) &\leq \phi(\tilde{x}(t + T + \Delta t)) + \int_{t + \Delta t}^{t + T + \Delta t} l(\tilde{x}, \tilde{u}, \tau) d\tau \\ &\leq V^*(x(t)) - \int_t^{t + \Delta t} l(x^*, u^*, \tau) d\tau. \end{aligned} \quad (30)$$

Step 3: Terminal Conditions

For the switched-system dynamics given by Eq. (17), the terminal cost satisfies the following condition:

$$\phi(f(x, \kappa_f(x))) - \phi(x) \leq -l(x, \kappa_f(x), t), \quad (31)$$

which can be achieved through:

- SLQ-based linearization;
- Riccati solution for P ;
- Contact-phase invariant set \mathcal{X}_f .

Step 4: Switched System Stability

The switching sequence ensures the following:

$$V^*(x(t_k^+)) \leq V^*(x(t_k^-)). \quad (32)$$

Step 5: Terrain Robustness

Define a robust Lyapunov function as follows:

$$V_r(x) = V^*(x) + \frac{1}{2\gamma} \tilde{\mu}^2, \quad (33)$$

whose derivative satisfies the condition given by:

$$\dot{V}_r \leq -\alpha \|x\|^2 + \beta \|\tilde{\mu}\| \|x\|. \quad (34)$$

Combining Steps 1–5 with LaSalle's principle proves stability within the specified boundaries.

The stability guarantees hold under the following conditions.

The analysis extends to:

- High-slip conditions ($s > 30\%$) with anti-slip control, which are defined by:

$$T_i^{slip} = K_p(s_i - s_{safe}) + K_i \int (s_i - s_{safe}) dt; \quad (35)$$

- Rough terrain with switching frequency limit, which is defined by:

$$f_{switch} \leq \frac{1}{2\tau_s} + \frac{v_{des}}{2L_c}. \quad (36)$$

3.6 Constraints

To ensure the physical feasibility of a wheeled-legged vehicle during motion, constraints must be applied to the optimization variables. In the switched-system MPC, different constraints can be set for each subsystem. This paper defines different constraints for each leg depending on whether the wheel is in contact with the ground. The constraint setup for the switched system is illustrated in Figure 2. In Section 2, the modeling of the five subsystems of the wheeled-legged vehicle, including the wheel dynamics model, tire model, and skid-steer kinematics model, which are enforced as equality constraints in the MPC, is presented in detail. However, the constraints introduced in the following also need to be applied.

3.6.1 Friction Cone Constraint

In the contact phase, the Coulomb friction limit must be satisfied to ensure effective contact forces, yielding the following inequality constraint:

$$\mu \cdot F_i^z \geq \sqrt{(F_i^x)^2 + (F_i^y)^2}, \quad (37)$$

where μ is the ground friction coefficient.

The above inequality enforces Coulomb's friction law, ensuring the resultant tangential force (F_i^x, F_i^y) never exceeds the maximum static friction of μF_i^z , thus avoiding wheel slippage.

3.6.2 Zero Velocity Constraint

During the contact phase, the vertical velocity of the CoW relative to the terrain normal direction is zero, which can be expressed by:

$$\mathbf{v}_{f_i} \cdot \vec{n} = 0, \quad (38)$$

where \vec{n} denotes the unit normal vector of the terrain.

This constraint guarantees the non-penetration condition by eliminating relative motion along the contact normal direction, which is essential for ensuring stable ground contact.

3.6.3 Zero Force Constraint

During the swing phase of the wheel, the contact force at the wheel end is zero, which yields the following equality constraint:

$$\lambda_i = 0. \quad (39)$$

This nullifies all ground reaction force components when the leg is airborne, effectively representing the physical detachment between the wheel and the terrain during the swing phase.

3.6.4 Normal Velocity Constraint

When a wheeled-legged vehicle does not follow a pre-designed trajectory or a planned gait, it can still operate using standardized gaits generated in response to keyboard input or remote control commands. These gaits are characterized by fixed leg-lifting heights and durations. The desired velocity of the CoW is obtained through cubic polynomial fitting. To this end, a constraint is applied to track the vertical velocity of the CoW as follows:

$$v_{fi}^z - v_{ref}^z = 0, \quad (40)$$

where v_{fi}^z is the vertical velocity of the CoW obtained through forward kinematics, and v_{ref}^z is the desired vertical velocity of the CoWs determined by cubic polynomial fitting.

This enables precise foot trajectory tracking during the swing phase, where the cubic polynomial generates smooth vertical motion profiles for leg lifting and lowering.

4 Experimental Results and Discussion

The proposed trajectory optimization algorithms were validated through real-world experiments to demonstrate their versatility in handling multiple interfaces and adaptability across various complex terrains. The experimental details are provided below, with an accompanying video footage showcasing the results.

4.1 Experimental Setup

The experiments were conducted on the LegoWheel platform, which was equipped with 12 torque-controlled motors and a motion controller (Intel i9-14900). As shown in Figure 3, unlike traditional Wheeled-Legged robots, the fully torque-controlled Wheeled-Legged vehicle, the LegoWheel, was equipped with only three motors per leg, located at the hip, knee, and wheel joints. This design provided the vehicle with a total of 12 degrees of freedom in its drive system. All algorithms were executed on this controller. The MPC solver used OCS2 [35], an open-source nonlinear MPC solver designed for hybrid systems, to generate control signals at a frequency of 100 Hz. For kinematics and dynamics modeling, this study adopted the open-source rigid body dynamics library Pinocchio [36]. The tracking controller adopted the whole-body control (WBC) method [37,38], which optimized the solution for joint and wheel torques. The WBC solver used the qpOASES library [39], an open-source C++ QP solver, with a solving frequency set at 500 Hz. All controllers shared the same state estimator [40] running at a frequency of 500 Hz.

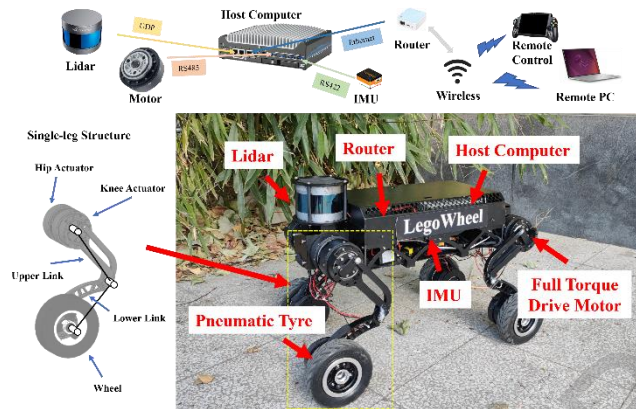


Figure 3 A physical prototype of a wheeled-legged vehicle system, LegoWheel.

4.2 Linear and Angular Velocity Tracking

Random 1–50 Hz command inputs were used in the experiments to validate the speed tracking performance of the proposed algorithm. Multiple sets of experimental tests were conducted on a Tile Floor with an indoor friction coefficient of approximately 0.5, and representative experiments were selected. A precise linear and angular velocity tracking in the terrain-independent mode is illustrated in Figure 4, where sign reversal tests the transient response.

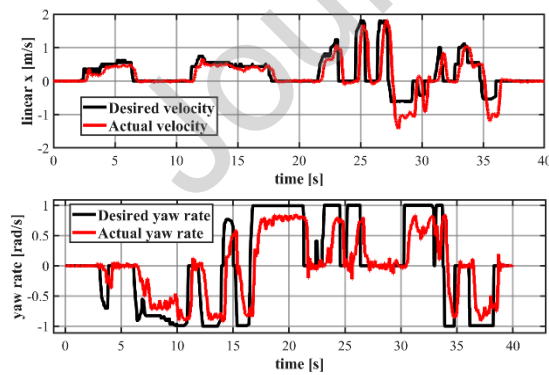


Figure 4 The command tracking performance: (a) linear velocity, (b) Angular velocity.

The experimental results revealed three key findings. First, the measured velocities (red curves in Figure 4) closely match the commanded trajectories (black curves in Figure 4), confirming the effectiveness of the proposed optimization algorithm. Second, observable phase delays occurred during high-gradient command transitions, primarily due to the controller bandwidth limitations and mechanical system inertia. Third, the system maintained robust performance across the entire tested frequency range.

4.3 Tracking Trajectories for Stair Climbing

The stair climbing experiment provided comprehensive validation of the proposed trajectory tracking framework, particularly focusing on 3D motion control. The trajectory comparison during the stair climbing maneuver is presented in Figure 5. As shown in Figure 5, the system achieved precise tracking for both the centroid and wheel position trajectories, closely matching the NLP-generated reference paths. This excellent tracking performance could be attributed to several key technical implementations.

First, regarding the state estimation, this study employed the PV-LIO algorithm [41] for global positioning combined with real-time drift correction. This addressed the critical challenge of vertical position estimation, which could directly impact the standing stability in wheeled-legged systems. The results indicated that despite environmental noise causing occasional vertical estimation errors, the control system could maintain robust performance throughout the stair climbing maneuver.

Second, the trajectory tracking results revealed three key characteristics of the proposed algorithm: (1) its ability to effectively compensate for vertical estimation errors while maintaining trajectory continuity; (2) its capability to precisely follow desired trajectories through real-time wheel motion adjustments; (3) its property of successful demonstration of dynamic adaptability throughout the entire stair crossing sequence.

The results demonstrated the controller's robustness to sensing uncertainties and measurement noise in complex 3D environments. Notably, the stair negotiation task validated the practical effectiveness of the proposed approach for real-world applications requiring precise motion control in challenging terrains.

Although successful, this experiment highlighted the system's dependence on accurate vertical position estimation. Specifically, in scenarios with complete perception loss, the proposed framework would require substantial modifications to maintain comparable performance.

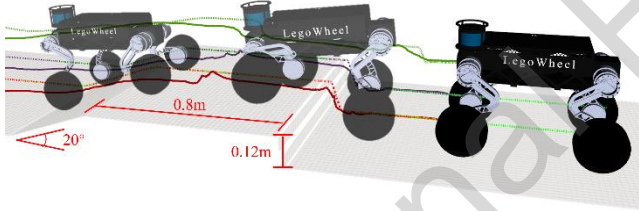


Figure 5 Trajectory comparison during the stair climbing maneuver.

4.4 Trot Gait

In this experiment, the commonly used trot gait, which is also known as diagonal gait, in traditional quadruped robots and wheeled-legged robots was tested by setting a fixed swing time and height for each leg [1]. Multiple sets of experimental tests were performed on a Tile Floor with an indoor friction coefficient of approximately 0.5. As shown in Figure 6, the swing height was 0.1 m, and the swing time was 0.5 s for one experiment, in comparison to a mode where all legs remained in continuous contact with the ground at the same forward speed (0.3 m/s). The experiment analyzed the platform's roll and pitch dynamics. The results indicated that due to the presence of wheels and wheel motors, the mass of the wheels relative to the body was high, causing significant roll and pitch changes during continuous stepping actions. Conversely, the mode of movement where legs were in continuous contact with the ground kept the body more stable during motion. Table 1 presents the comparison results of performance metrics between the leg swing and leg standing modes. Moreover, stability analysis showed that changes in the pitch and roll values were controllable under moderately complex terrains, but more noticeable during fast continuous stepping actions. This indicated that unnecessary lifting of legs should be minimized to reduce dynamic instability, further pointing out the importance of optimized gait strategies in improving stability and reducing energy consumption.

The torque comparisons showed the RMS values for hip and knee joints were as follows: 1.14/6.53 N·m (swing) vs 0.27/3.39 N·m (standing); this confirmed the energy efficiency advantage of standing mode. In comparison, the skid-steer contact steering method exhibited superior performance in maintaining stability and reducing energy consumption. The

results of this experiment highlighted the importance of the trade-off between flexibility and stability in wheeled-legged vehicles, further emphasizing the necessity of employing contact-based movement strategies in certain scenarios.

Table 1 Comparison results of the performance metrics for the leg swing and leg standing experiments

Metric	Leg Swing	Leg Standing
Roll angle variation (rad)	0.0373	0.0136
Pitch angle variation (rad)	0.0405	0.0132
RMS. HFE torque (Nm)	1.1432	0.2731
RMS. KFE torque (Nm)	6.5284	3.3907
Stability	Low	High
Energy efficiency	Low	High

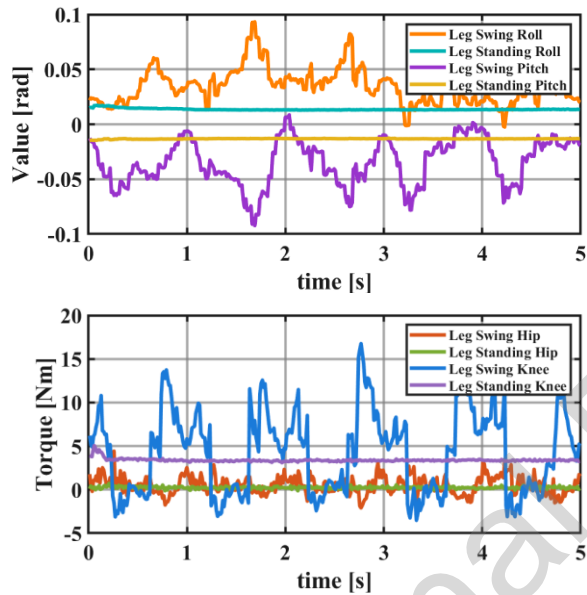


Figure 6 Comparison results of the trot gait experiment: roll and pitch (Top), torque of the left front leg's hip and knee joint motors with all legs standing (Bottom).

4.5 Tracking Trajectories for Trench Crossing

During this experiment, the platform could effectively cross the ditch based on the planned trajectory, avoiding wheel entrapment, which was not achievable by a perception-free controller trained using RL. The ditch-crossing experiment also demonstrated that the platform could successfully cross the ditch via the planned 3D trajectory, as shown in Figure 7, thus avoiding the risk of wheel entrapment. The trajectory tracking graph indicated the platform's stable motion within the ditch, highlighting the effectiveness of contact force distribution and trajectory planning. Since the platform's leg length was only 0.15 m and the normal step length was shorter than 0.15 m, the platform lowered its CoM during the step-preparation phase to provide a longer stepping distance. In addition, the wheel mass caused body tilting during the leg-lifting process, indicating the need to raise the body on the lifting side through the support of the other three legs. Thus, the proposed control framework played a key role in dynamically adjusting contact forces, enabling the vehicle to remain stable even under partial support loss. This experiment further validated the reliability of the control system in handling complex obstacles and emphasized the importance of real-time trajectory optimization for system stability.

The ditch-crossing capability originated from two inherent constraints: (1) the maximum negotiable gap was limited by the leg kinematics, and (2) the planning latency increased with terrain complexity due to the NLP solver's computational demands.

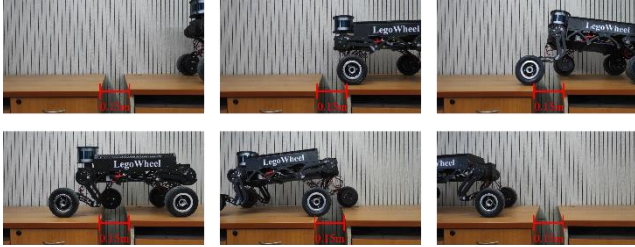


Figure 7 The platform tracking an offline motion trajectory based on terrain perception and crossing a 0.15-m-long ditch (the same diameter as the wheels).

4.6 Dynamic Adaptation to Complex Terrain: Evaluation of Vehicle Stability and Control

In this experiment, the controller's environmental adaptability was evaluated as the vehicle successfully drove on a 25° -inclined surface. As depicted in Figure 8, in perception-free mode, the vehicle smoothly traversed a total length of 6.4 m on the ramped surface, adaptively adjusting its posture throughout the passage. The experimental setup comprised a 25° , 2.2-m-long ascent, a 2-m-long level segment, and a 25° , 2.2-m-long descent, during which the vehicle drove continuously. In Figure 8, the x -axis denotes the vehicle's longitudinal position relative to the starting point, and the y -axis indicates the roll angle; the red line illustrates roll angle variations throughout the transit. During the transit, the maximum and minimum roll angles were 0.0487 rad and -0.0533 rad, respectively, demonstrating the controller's capability and robustness in navigating challenging terrains.

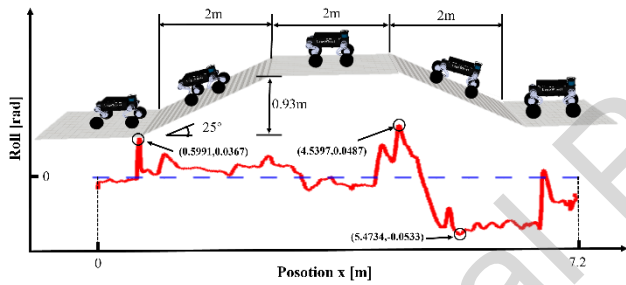


Figure 8 The results of the perception-free adaptation test.

4.7 Enhanced Velocity Tracking Through Integrated Wheel Dynamics

The proposed method was compared with the conventional approach used in wheeled-legged robots, where wheels are simplified as moving contact points [20]. Since traditional wheeled-legged robots achieve steering through HAA joints, this comparison focused exclusively on the longitudinal velocity tracking results, excluding steering. Multiple sets of experimental tests were conducted on a tile floor with an indoor friction coefficient of approximately 0.5, as shown in Figure 9. The traditional motion control method that disregarded tire dynamics and wheel-ground contact tracked only the speed of the moving contact point, resulting in no feedforward torque. Even with high gains on the wheel motor speed, direct velocity tracking failed to achieve the desired speed. In contrast, the proposed method, which integrated rigid body dynamics with wheel dynamics, could directly optimize the desired wheel speed and torque, thus enabling faster and more stable tracking of the target speed.

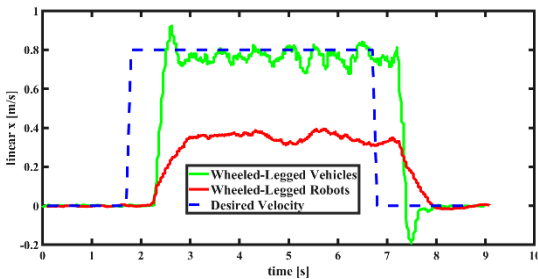


Figure 9 Comparative velocity tracking performance: proposed method (green) vs. conventional contact-point model (red), tracking a 0.8 m/s reference trajectory (blue dashed).

4.8 Energy Consumption Comparison in Straight-line Motion

To evaluate the energy-saving performance, this study conducted quantitative comparative simulations. For fair comparison, HAA joints were added to the LegoWheel simulation model while keeping other kinematic and dynamic parameters identical, with the ground friction coefficient set to 0.6. The maximum torque of the joint and wheel motors was set to 33.5 Nm. The proposed method was compared with the approach that simplified wheels as moving contact points and included HAA joints [20]; the vehicle response data were recorded during the experiments. Since actuator energy consumption was proportional to the output torque, torque comparison was used as an approximation of energy consumption comparison.

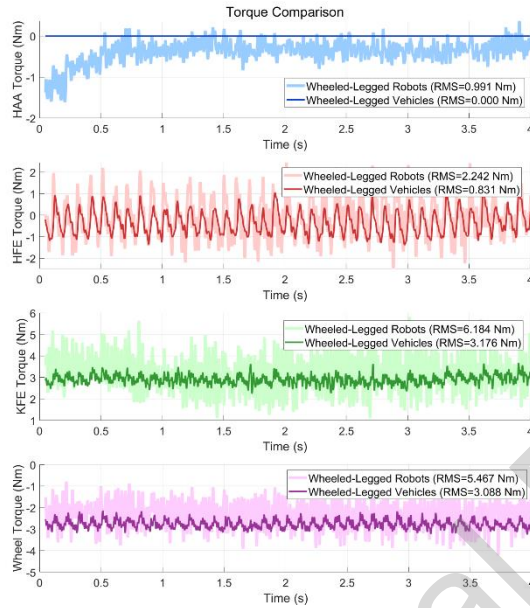


Figure 10 Joint torque comparison results obtained during straight-line motion. *For clarity, the data in the figure have been filtered using a 4th-order Butterworth low-pass filter with a cutoff frequency of 5 Hz.*

In this experiment, multiple trials were performed, with data recorded over 4-s intervals when the average velocity stabilized at 1 m/s. Notably, the wheel-legged robot with the HAA joints required significant torque from the HAA motors to maintain body stability during straight-line motion. Without sufficient torque, the wheels could not remain directly beneath the chassis, causing a lateral force imbalance at wheel contacts. The substantial leg length further amplified this torque requirement. In addition, insufficient HAA torque caused delayed correction, resulting in continuous leg splaying and eventual controller failure.

During the experiment, when the HAA PID gains were set to $k_p = 16$ and $k_d = 2$, the controller failed as leg deviation increased progressively. Stable performance was achieved only with higher gains ($k_p = 200$, $k_d = 10$), which enabled timely correction and sustained normal operation.

Representative experimental data are presented in Figure 10, where the HAA PID gains were set to $k_p = 200$ and $k_d = 10$, the other joint motors had $k_p = 20$ and $k_d = 2$, and the wheel motors had $k_p = 0$ and $k_d = 1$. As shown in Table 2, the proposed method effectively eliminated the need for the HAA motors while maintaining identical parameters for the other motors. This not only simplified the mechanical structure but also reduced the torque requirements for all motors, resulting in an overall motor energy consumption reduction of 52.33%.

Table 2 Torque comparison results of the straight-line motion experiment.

Metric	Wheeled-legged robots	Wheeled-legged vehicles
--------	-----------------------	-------------------------

RMS. HAA torque (Nm)	0.991	0
MAX. HAA torque (Nm)	4.277	0
RMS. HFE torque (Nm)	2.242	0.831
MAX. HFE torque (Nm)	10.686	2.938
RMS. KFE torque (Nm)	6.184	3.176
MAX. KFE torque (Nm)	30.336	8.027
RMS. Wheel torque (Nm)	5.467	3.088
MAX. Wheel torque (Nm)	33.455	8.533

4.9 Energy Consumption Comparison in Spot Turning

Next, the energy-saving performance was evaluated during spot-turning maneuvers. Using identical dynamic parameters (the ground friction coefficient of 0.6) except for the added HAA joints, it was found that impedance control (simultaneously commanding the desired position, velocity, and torque) in the simplified contact point algorithm frequently caused instability [20]. Furthermore, the high stiffness from position commands made impact absorption difficult, causing significant CoM variations. After tuning, stable trot and walk gaits were achieved at $k_p = 0$ and $k_d = 3$. However, skid-steering required higher k_p values for robustness due to the varying ground friction and challenging contact force estimation.

Multiple experiments were conducted with the wheel-legged robot's PID gains of $k_p = 0$ and $k_d = 3$, and the wheeled vehicle's PID gains of $k_p = 20$ and $k_d = 2$. The maximum torque of both the joint and wheel motors was set to 33.5 Nm. During the experiment, data were recorded at 4-s intervals when the platform's angular velocity averaged 2.5 rad/s. Representative experimental data are depicted in Figure 11, and comparison results are presented in Table 3.

Table 3 Torque Comparison Results of the Spot Turning Experiment.

Metric	Wheeled-legged robots	Wheeled-legged vehicles
RMS. HAA torque (Nm)	5.836	0
Max. HAA torque (Nm)	33.5	0
RMS. HFE torque (Nm)	4.492	7.542
Max. HFE torque (Nm)	31.946	16.846
RMS. KFE torque (Nm)	5.745	2.354
Max. KFE torque (Nm)	33.500	7.946
RMS. Wheel torque (Nm)	5.769	2.506
Max. Wheel torque (Nm)	33.500	8.269

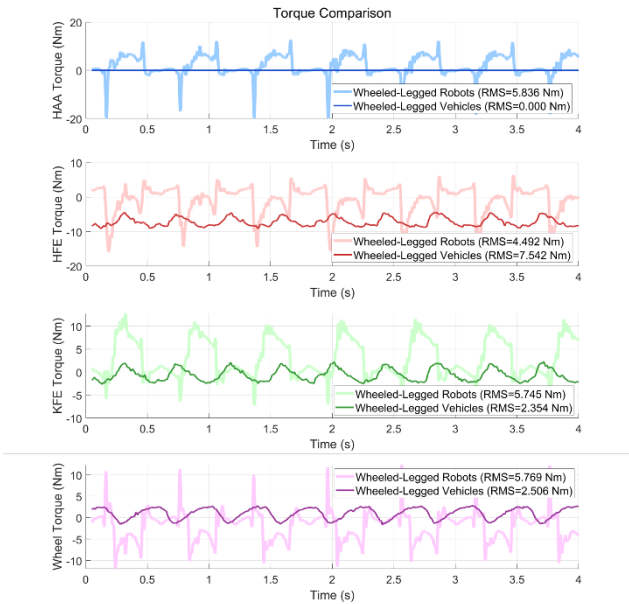


Figure 11 Joint torque comparison during spot turning. For clarity, the data in the figure have been filtered using a 4th-order Butterworth low-pass filter with a cutoff frequency of 5 Hz.

Notably, in conventional legged motion, hip joints typically require less torque than knee joints. However, during skid-steering, hip joints require substantially higher torque. The results indicated that the proposed method could achieve a 43.22% reduction in the total motor energy consumption during in-place turning scenarios. Moreover, additional experiments revealed that the torque required for skid-steering increased with the friction coefficient values, thus making wheeled vehicle steering more challenging.

5 Conclusions

This study presents a comprehensive experimental validation of the proposed innovative trajectory optimization algorithm for skid-steer wheeled-legged vehicles, and quantitative results demonstrate its superior performance across diverse terrains. The controller achieved precise velocity tracking. The stair climbing experiment revealed that the 3D trajectory tracking accuracy was within 2 cm of reference paths. In addition, the proposed approach demonstrated significant energy efficiency advantages, showing a 52.33% reduction in motor energy consumption during straight-line motion compared to conventional methods.

The system's terrain adaptability was rigorously validated across multiple experimental scenarios. The slope navigation test demonstrated stable operation on 25° inclines with roll angle variations limited to ± 0.0533 rad. The platform successfully crossed ditches equal to its wheel diameter (0.15 m) through optimized trajectory planning. Moreover, torque comparisons revealed a 43.22% energy consumption reduction during spot turning maneuvers. These quantitative results collectively demonstrated the proposed algorithm's effectiveness in balancing mobility and energy efficiency across various complex terrains.

The validated capabilities make this system particularly suitable for three key scenarios:

(1) Inspection in complex industrial facilities (e.g., refineries with staircases and pipelines). The results have indicated that in these scenarios, the proposed contact-adaptive steering outperforms traditional skid-steer vehicles in confined spaces.

(2) Disaster response scenarios that require traversing collapsed buildings. These scenarios can particularly benefit from the proposed method's combined advantages of wheeled efficiency and legged mobility.

(3) Agricultural operations on uneven terrains, where perception-free control maintains stability despite ground irregularities.

The experimental results have revealed the following limitations of the current algorithm:

(1) The nonlinear programming-based offline trajectory computation is computationally intensive, and real-time performance cannot be guaranteed.

(2) The performance of the proposed algorithm is highly dependent on perception and localization when operating on complex terrain; therefore, loss of perception could disable gait pre-planning.

(3) The results of the stationary steering experiments have demonstrated increased difficulty when the proposed algorithm operates on high-friction terrain.

Future research will focus on the following aspects. First, RL could be integrated into trajectory planning to improve real-time performance in complex working conditions. Second, the state estimation accuracy could be enhanced to increase controller robustness under the condition of inaccurate state data. Finally, the proposed algorithm could be further optimized to minimize small-radius steering on high-friction terrain.

Authors' Contributions

MX was responsible for theoretical modeling, manuscript writing, and experimental implementation; ZY, CX, and KW assisted in completing the experiments; YZ and YQ provided consultation and suggestions for manuscript preparation. All authors read and approved the final version of the manuscript.

Authors' Information

Mingfan Xu received his B.Sc. degree in vehicle engineering from *Hebei University of Engineering, Handan, China*, in 2019. He is currently pursuing his Ph.D. degree at the *School of Mechanical Engineering, Beijing Institute of Technology, China*. His current research interests include dynamic control for wheel-legged vehicles.

Ziyi Yang received his B.Sc. degree from the *Hebei University of Technology, China*, in 2024. He is currently pursuing his M.Sc. degree at the *School of Mechanical Engineering, Beijing Institute of Technology, China*. His research interests include optimal trajectory planning and control for wheel-legged robots.

Chuyan Xu received his B.Sc. degree from *Beijing Institute of Technology, China*, in 2024. He is currently pursuing his M.Sc. degree at the *School of Mechanical Engineering, Beijing Institute of Technology, China*. His research interests include wheel-legged multi-mode vehicle dynamics and control.

Kui Wang received his B.E. degree in automotive engineering from *Jilin University, China*, in 2023. He is currently pursuing his M.E. degree at the *Institute of Vibration and Noise Research, School of Mechanical and Vehicle Engineering, Beijing Institute of Technology, China*.

Yu Zhang received his Ph.D. degree in mechanical engineering from the *Beijing Institute of Technology, China*, in 2023. He is currently a postdoctoral researcher at the *School of Mechanical Engineering, Beijing Institute of Technology, China*. His current research interests include decision-making and dynamic control for intelligent vehicles.

Yechen Qin received the B.Sc. and Ph.D. degrees in mechanical engineering from the *Beijing Institute of Technology, China*, in 2010 and 2016, respectively. From 2013 to 2014, he was a visiting Ph.D. student at *Texas A&M University, USA*. He also worked as a postdoctoral research fellow and a visiting scholar at the *Beijing Institute of Technology, China*, and the *University of Waterloo, Canada*. He is currently an associate professor at the *Beijing Institute of Technology, China*. His research focuses on autonomous vehicle dynamic control. He also serves as an Associate Editor for the IEEE Transactions on Vehicular Technology and IEEE Transactions on Intelligent Vehicles.

Competing Interests

The authors declare no competing financial interests.

Acknowledgements

Not applicable.

Funding

Supported by National Natural Science Foundation of China (Grant No. 52272386), the Fundamental Research Funds for the Central Universities, the China Postdoctoral Science Foundation (Grant Nod. 2024T171128 and 2024M764122), and the Postdoctoral Fellowship Program of CPSF (Grant No. GZC20233402).

References

- [1] M Bjelonic, P K Sankar, C D Bellicoso, et al. Rolling in the deep--hybrid locomotion for wheeled-legged robots using online trajectory optimization. *IEEE Robotics and Automation Letters*, 2020, 5(2): 3626-3633.

- [2] J Lee, M Bjelonic, A Reske, et al. Learning robust autonomous navigation and locomotion for wheeled-legged robots. *Science Robotics*, 2024, 9(89): eadi9641.
- [3] Y C Qin, Z W Zhu, Y P Zhou, et al. Bi-Level Optimization for Closed-Loop Model Reference Adaptive Vibration Control in Wheeled-Legged Multimode Vehicles. *IEEE Transactions on Industrial Electronics*, 2025, 70(12): 12545-12554.
- [4] J Kim, C D Crane, J Kim. Development of the autonomous navigation algorithm based on the geometric method for skid steering vehicles: Convergence of skid steering and pure pursuit methods using compensation coefficients. *Proceedings of the 2022 22nd International Conference on Control, Automation and Systems*, Seoul, South Korea, November 27-30, 2022: 1996-2001.
- [5] W H Hao, L J Han, H Liu, et al. Skid steering control and wheel-centred trajectory planning for wheel-legged robots. *Proceedings of the 2023 5th International Conference on Robotics, Intelligent Control and Artificial Intelligence*, Shanghai, China, December 8-10, 2023: 149-152.
- [6] Z Dorbetkhany, A Murbabulatov, M Rubagotti, et al. Spatial-based model predictive path following control for skid steering mobile robots. *Proceedings of the 2022 18th IEEE/ASME International Conference on Mechatronic and Embedded Systems and Applications*, Philadelphia, PA, USA, November 14-16, 2022: 1-6.
- [7] T W Kang, S W Cho, C H Park, et al. Linear lateral motion model for urban delivery skid steering robot. *Proceedings of the 2022 22nd International Conference on Control, Automation and Systems*, Seoul, South Korea, November 27-30, 2022: 960-964.
- [8] J L Martínez, J Morales, M Sánchez, et al. ICR-based kinematics for wheeled skid-steer vehicles on firm slopes. *Proceedings of the 2024 IEEE/RSJ International Conference on Intelligent Robots and Systems*, Dubai, UAE, May 13-17, 2024: 1322-1328.
- [9] R X Cao, J Gu, C Yu, et al. OmniWheg: An omnidirectional wheel-leg transformable robot. *Proceedings of the 2022 IEEE/RSJ International Conference on Intelligent Robots and Systems*, Kyoto, Japan, October 23-27, 2022: 5626-5631.
- [10] E Jelavic, K X Qu, F Farshidian, et al. LSTP: Long short-term motion planning for legged and legged-wheeled systems. *IEEE Transactions on Robotics*, 2023, 39(6): 4190-4210.
- [11] A Trivedi, M Zolotas, A Abbas, et al. A probabilistic motion model for skid-steer wheeled mobile robot navigation on off-road terrains. *Proceedings of the 2024 IEEE International Conference on Robotics and Automation*, Singapore, May 13-17, 2024: 12599-12605.
- [12] Y Tan, X Su, C Shen, et al. Motion tracking control of six-wheel skid-steering electric vehicles via two-level-sequence-based integrated algorithm. *IEEE Transactions on Industrial Electronics*, 2024, 71(11): 14937-14945.
- [13] M Effati, K Skonieczny, T Freiman, et al. An equivalent time-optimal problem to find energy-optimal paths for skid-steer rovers. *Proceedings of the 2022 IEEE/RSJ International Conference on Intelligent Robots and Systems*, Kyoto, Japan, October 23-27, 2022: 13341-13346.
- [14] R Xiong, L Li, C Zhang, et al. Path tracking of a four-wheel independently driven skid steer robotic vehicle through a cascaded NTSM-PID control method. *IEEE Transactions on Instrumentation and Measurement*, 2022, 71: 1-11.
- [15] X Zuo, M Zhang, M Wang, et al. Visual-based kinematics and pose estimation for skid-steering robots. *IEEE Transactions on Automation Science and Engineering*, 2024, 21(1): 91-105.
- [16] M Bjelonic, R Grandia, O Harley, et al. Whole-body mpc and online gait sequence generation for wheeled-legged robots. *Proceedings of the 2021 IEEE/RSJ International Conference on Intelligent Robots and Systems*, Prague, Czech Republic, September 27-October 1, 2021: 8388-8395.
- [17] Z Wei, Z Q Cai, Z Y Yu, et al. BiTSpoke: A leg-wheel robot with single-motor driven actively-transformable spoke wheels. *IEEE Robotics and Automation Letters*, 2025, 10(5): 4874-4881.
- [18] P C Huang, I C Chang, W S Yu, et al. Body velocity estimation in a leg-wheel transformable robot without a priori knowledge of leg-wheel ground contacts. *Proceedings of the 2024 IEEE International Conference on Robotics and Automation*, Yokohama, Japan, May 13-17, 2024: 11349-11355.
- [19] M Hosseini, D Rodriguez, S Behnke. Dynamic hybrid locomotion and jumping for wheeled-legged quadrupeds. *Proceedings of the 2023 IEEE/RSJ International Conference on Intelligent Robots and Systems*, Detroit, MI, USA, October 1-5, 2023: 793-799.
- [20] M Bjelonic, R Grandia, M Geilinger, et al. Offline motion libraries and online MPC for advanced mobility skills. *The International Journal of Robotics Research*, 2022, 41(9-10): 903-924.
- [21] D C Liu, J Z Wang, D W Shi, et al. Posture adjustment for a wheel-legged robotic system via leg force control with prescribed transient performance. *IEEE Transactions on Industrial Electronics*, 2023, 70(12): 12545-12554.
- [22] L X Zhao, Z G Yu, L Q Han, et al. Compliant motion control of wheel-legged humanoid robot on rough terrains. *IEEE/ASME Transactions on Mechatronics*, 2024, 29(3): 1949-1959.
- [23] Q Q Zhou, S C Yang, X Y Jiang, et al. Max: A wheeled-legged quadruped robot for multimodal agile locomotion. *IEEE Transactions on Automation Science and Engineering*, 2024, 21(4): 7562-7582.
- [24] Y Wang, T Chen, X W Rong, et al. Design and control of SKATER: A wheeled-bipedal robot with high-speed turning robustness and terrain adaptability. *IEEE/ASME Transactions on Mechatronics*, 2025, 30(2): 1310-1321.
- [25] A Mane, D Swart, J White, et al. Trajectory optimization formulation with smooth analytical derivatives for track-leg and wheel-leg ground robots. *Proceedings of the 2022 International Conference on Robotics and Automation*, Philadelphia, PA, USA, May 23-27, 2022: 5762-5768.
- [26] M Bjelonic, C D Bellicoso, M E Tiryaki, et al. Skating with a force controlled quadrupedal robot. *Proceedings of the 2018 IEEE/RSJ International Conference on Intelligent Robots and Systems*, Madrid, Spain, October 1-5, 2018: 7555-7561.
- [27] J Chen, R Qin, L Huang, et al. Unlocking versatile locomotion: A novel quadrupedal robot with 4-Dof's legs for roller skating. *Proceedings of the 2024 IEEE International Conference on Robotics and Automation*, Dubai, UAE, May 13-17, 2024: 8037-8043.
- [28] M Bjelonic, C D Bellicoso, Y de Viragh, et al. Keep rollin'--whole-body motion control and planning for wheeled quadrupedal robots. *IEEE Robotics and Automation Letters*, 2019, 4(2): 2116-2123.
- [29] E Vollenweider, M Bjelonic, V Klemm, et al. Advanced skills through multiple adversarial motion priors in reinforcement learning. *Proceedings of the 2023 IEEE International Conference on Robotics and Automation*, Singapore, May 29-June 2, 2023: 5120-5126.
- [30] D Robotics. DEEP Robotics "Lynx": All-terrain Off-road Robot. <https://www.deeprobotics.cn/robot/index/deeproboticslynx.html>, 2024.
- [31] UNITREE. Unitree B2W: four-legged wheeled robot dog. <https://www.unitree.com/cn/b2-w>, 2024.

-
- [32] F Jenelten, J He, F Farshidian, et al. DTC: Deep tracking control. *Science Robotics*, 2024, 9(86): eadh5401.
 - [33] X Zhang, S Yuan, X Yin, et al. Estimation of skid-steered wheeled vehicle states using STUKF with adaptive noise adjustment. *Applied Sciences*, 2021, 11(21): 10391.
 - [34] A W Winkler, C D Bellicoso, M Hutter, et al. Gait and trajectory optimization for legged systems through phase-based end-effector parameterization. *IEEE Robotics and Automation Letters*, 2018, 3(3): 1560-1567.
 - [35] F Farshidian. Optimal Control for Switched Systems Toolbox. <https://leggedrobotics.github.io/ocs2>, 2022.
 - [36] J Carpentier, G Saurel, G Buondonno, et al. The Pinocchio C++ library: A fast and flexible implementation of rigid body dynamics algorithms and their analytical derivatives. *Proceedings of the 2019 IEEE/SICE International Symposium on System Integration*, Paris, France, January 14-16, 2019: 614-619.
 - [37] C D Bellicoso, C Gehring, J Hwangbo, et al. Perception-less terrain adaptation through whole body control and hierarchical optimization. *Proceedings of the 2016 IEEE-RAS 16th International Conference on Humanoid Robots*, Cancún, Mexico, November 15-17, 2016: 558-564.
 - [38] C D Bellicoso, F Jenelten, P Fankhauser, et al. Dynamic locomotion and whole-body control for quadrupedal robots. *Proceedings of the 2017 IEEE/RSJ International Conference on Intelligent Robots and Systems*, Vancouver, BC, Canada, September 24-28, 2017: 3359-3365.
 - [39] H J Ferreau, C Kirches, A Potschka, et al. qpOASES: A parametric active-set algorithm for quadratic programming. *Mathematical Programming Computation*, 2014, 6: 327-363.
 - [40] M Hosseini, D Rodriguez, S Behnke. State estimation for hybrid locomotion of driving-stepping quadrupeds. *Proceedings of the 2022 Sixth IEEE International Conference on Robotic Computing*, Naples, Italy, December 5-7, 2022: 103-110.
 - [41] H ViktorTsoi. A probabilistic voxelmap-based LiDAR-Inertial Odometry. <https://github.com/HViktorTsoi/PV-LIO>, 202

Appendix

To ensure the reproducibility of the proposed method, this study provides the complete set of MPC weighting parameters used in the experiments. The state weighting matrix \mathbf{Q} and input weighting matrix \mathbf{R} are diagonal matrices, and their diagonal elements are provided in Tables 4 and 5, respectively.

Table 4 The MPC Weighting Parameters of the State Weighting Matrix.

Q	Weight
\mathbf{v}_x	500
\mathbf{v}_y	500
\mathbf{v}_z	100
$\boldsymbol{\omega}_x$	10
$\boldsymbol{\omega}_y$	30
$\boldsymbol{\omega}_z$	300
\mathbf{p}_x	5,000
\mathbf{p}_y	1,500
\mathbf{p}_z	1,500
$\boldsymbol{\theta}_x$	300
$\boldsymbol{\theta}_y$	200
$\boldsymbol{\theta}_z$	300
\mathbf{q}_{hip}	500
\mathbf{q}_{knee}	400
\mathbf{w}_i	1,000

Table 5 The MPC Weighting Parameters of the Input Weighting Matrix.

R	Weight
λ_x	10
λ_y	10
λ_z	1
\mathbf{u}_{hip}	80,000
\mathbf{u}_{knee}	80,000
\mathbf{a}	1
\mathbf{T}	1